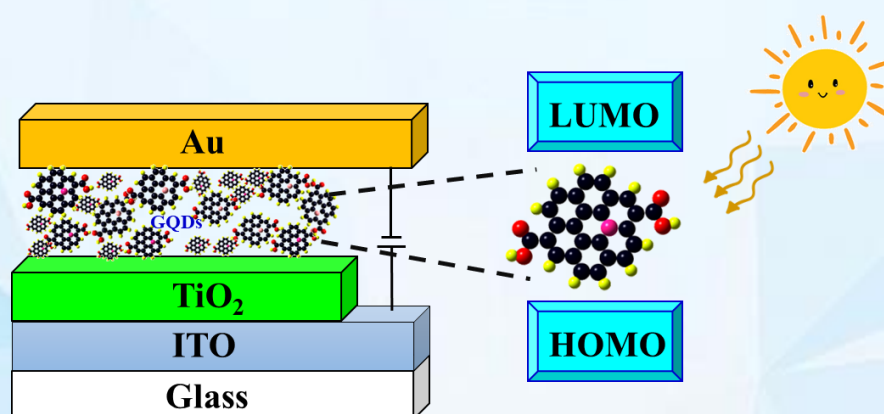


Chapter 5

Enhancement in power conversion efficiency of edge-functionalized graphene quantum dot through adatoms for solar cell applications



5.1 Introduction

The large-scale production of clean energy is an urgent need to compensate the world's need for electricity and reduction in climate change events. The possible solution for these needs may be third generation photovoltaic (PV) solar cells, because of their reduced cost with high efficiency and incredible potential for large-scale electricity production over globe [1]. The quantum dot solar cells (QDSCs) have shown great interest in recent years due to their characteristics such as use in low-cost solar cells, greater absorption coefficient, adjustable band gaps with shape and size etc. [2,3]. Moreover, lead and cadmium based quantum dots such as colloidal cadmium selenide (CdSe), lead sulfide (PbS), cadmium telluride (CdTe) and cesium lead iodide (CsPbI₃) exhibits excellent tunable optical properties with size and carries capacity to cross the Shockley-Queisser limit [4–6]. However, the presence of highly toxic elements like Pb and Cd in above stated solar cells limits their prominent applications as solar cells. Thus, there is an urgent need of low-toxic, eco-friendly and biocompatible alternate solar cell materials for large-scale production. Basically, the QDSCs were categorized in three distinct compositions based on their structure and characteristics: (a) Schottky junction solar cells exhibit metal-QD junction that gives rise to PV effect, (b) organic solar cells show the PV effect amongst QD-polymer junction, and (c) QDSCs consisting the junction of quantum dot and metal oxide semiconductor of large band gap together with the electrolyte [7–12]. It appears that structure is almost identical with the dye-sensitized solar cells (DSCs), having merely one alteration of occurrence of PV effect that arises amid redox electrolyte and dye-metal oxide semiconductor.

Carbon based quantum dots such as GQDs exhibiting a zero-dimensionality have been significantly considered as its prominent applications towards the optoelectronics, light emission and bio-sensing etc. [13]. Furthermore, GQDs have gained considerable attraction by the researchers in the field of solar cells for implementation in dye sensitized solar cells to overcome the problems like toxicity, stability and biocompatibility appears in traditional solar cells [13]. Additionally, GQDs exhibit suitable absorption properties for high-efficient solar cells to harvest the light energy due to their confinement effect, edge effects, band gap tuning by size and shape. Recently, different types of carbon dots (CDs) and GQDs have been studied for solar cell applications [14]. So far, GQDs found their employment in material as hole transport layer (HTL) and semiconductor/GQDs heterojunction solar cell. The doping of nitrogen in carbon dots

is done by Zhang et al. [15] to study the optoelectronic properties along with 0.13% power conversion efficiency (PCE). Furthermore, Wang et al. [16] designed solar cells based on nitrogen doped CDs with power conversion efficiency of 0.79%. However, the efficiency reflects the need of improvement which is still in progress by the researchers. The heteroatoms significantly improve the electronic and optical properties of GQDs for high efficient solar energy conversion [17]. Additionally, functionalization of GQDs at the edges (presence of oxygen) influences in luminescence excitation and band gap [18,19]. Researches on polyaromatic hydrocarbons (PAH) have shown great interest towards their consideration for ideal GQDs. This is attributed to the attached honeycomb structure of PAH that are made up of tiny graphene fragments where hydrogen atoms lead to confinement in all directions by passivation of the dangling bonds [20–26]. These studies motivated to investigate the electronic and optoelectronic properties for harvesting the solar energy through doping of heteroatoms like boron, nitrogen and phosphorous to carboxyl functionalized GQD using density functional theory (DFT) based on first principles study. In present investigation, we have substituted individually the nitrogen, boron and phosphorous atoms in place of carbon of GQD with carboxyl functionalization named as “COOH-GQD” to get better electronic, optical and absorption properties for utilization in QDSCs.

5.2 Computational Details

The influence in COOH-GQD by doping of boron (B), nitrogen (N) and phosphorous (P) atoms were studied by performing the DFT calculations. Structural minimization of pristine and doped COOH-GQD was governed by B3LYP hybrid functional with basis set of 6-31G in the Gaussian09 suite of program [27–29]. The global minima of considered geometries were obtained by calculating the vibrational frequencies. Moreover, the single point energy calculation was performed for doped and pristine COOH-GQDs to get better accuracy in the energy. Electronic properties were investigated by means of the frontier molecular orbitals and band gap (E_g) which was further seen by GaussView software. Subsequent to geometry optimization, the time-dependent density functional theory (TD-DFT) was incorporated together with integral equation formalism model (IEFPCM), for investigation of molecular UV–Vis absorption spectra and electronic transitions in the systems. The self-consistent reaction field (SCRF) method was

used to consider the solvent effect in the framework of Polarizable Continuum Model (PCM) which accomplishes calculation of reaction field under IEFPCM method [30]. Macroscopic properties like dielectric constant (ϵ), surface tension etc. illustrates the solvent effects at 298 K. We have considered water as a solvent in present study having ϵ of 78.3. Moreover, the polarization of selected solvent is determined by surface charge density onto the shell of cavity and generates the electric field within cavity [31–33]. The UV–Vis spectrum was obtained with addition of water as a solvent. Following, solar efficiency was calculated by the following empirical relation to understand the implementation of doped/undoped COOH-GQDs to the QDSCs [34]:

$$\eta = \frac{FFJ_{sc}V_{oc}}{P_{in}} \quad (5.1)$$

Where, V_{oc} is open circuit voltage determined through the maximum voltage for solar cell once current turns to zero and is given by the following equation [35-37]:

$$V_{oc} = E_{LUMO}^{GQDs} - E_{CB}^{TiO_2} \quad (5.2)$$

The V_{oc} is nothing but the variation among the LUMO level of GQDs behaving as a donor and minimum energy of conduction band of TiO_2 behaving as an acceptor and depends on the light-generated current and saturation. Additionally, open circuit voltage gives the quantity of recombination process in device.

FF is the abbreviation for fill factor, which is related with V_{oc} and short-circuit current (I_{sc}) and obtained by following relation [35-37]:

$$FF = \frac{\vartheta_{oc} - \ln(\vartheta_{oc} + 0.72)}{\vartheta_{oc} + 1}; \quad \vartheta_{oc} = \frac{q \times V_{oc}}{k_B T} \quad (5.3)$$

Where ϑ_{oc} is the normalized V_{oc} [38].

Further, the light harvesting efficiency (LHE) is an important variable to optimize the short-circuit current density (J_{sc}), providing the higher efficiency for QDSCs. The J_{sc} is the current density once solar cell attains zero voltage. LHE is also known as absorptance (A) which is determined by the segment of strength in absorption of light at a certain wavelength within QDSCs or DSSCs [39].

$$LHE = A = \frac{I_{abs}}{I_o} \quad (5.4)$$

Where I_{abs} and I_o denotes the absorbed and incident intensity, respectively. Moreover, incident photon to current conversion efficiency (IPCE) is being directly proportional to the LHE and can be given by the following formula [40]:

$$IPCE = (LHE)\varphi\eta_c = A\varphi\eta_c \quad (5.5)$$

Where, η_c determines the efficiency of photoanode charge collection and φ denotes the quantum yield of charge injection. Using expressions (5.4) and (5.5) of LHE and IPCE respectively, the short-circuit current density (J_{sc}) can be given by the following expression [41]:

$$J_{sc} = \int q A\varphi\eta_c(E)I_{sun}(E)dE \quad (5.6)$$

where q is the charge, and $I_{sun}(E)$ represents photon flux density utilized arising out of AM1.5G spectrum. For GQDs, φ and η_c relies feebly on absorption wavelength (λ), which leads to determine equation (5.6) in terms of the following relation [41]:

$$J_{sc} = \int_0^\infty q A(E)I_{sun}(E)dE \quad (5.7)$$

Here, J_{sc} counts on different parameters such as solar cell region, incident light spectrum, absorption properties etc. In this study, we take $E_{CB}^{TiO_2} = -4.0\text{eV}$ [42-43].

5.3 Results and discussion

5.3.1 Structural Analysis

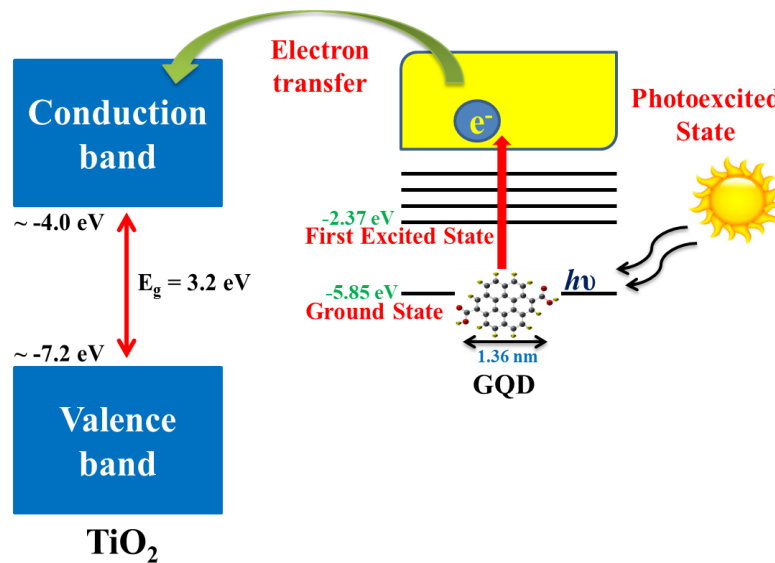


Figure 5.1: Illustration of photoinduced electron injection from a donor GQD to the surface of acceptor TiO_2 . The photon absorption benefits an electron from the GQD ground state with energy within E_g of TiO_2 , into the excited state.

The structural properties of GQD were initially obtained to demonstrate the basis of our calculations. After performing initial investigation on the configuration and characteristics of GQD, we performed these calculations with the substitutional doping of nitrogen, boron and phosphorous over GQD. In the present study, coronene ($C_{24}H_{12}$), comprising the strong ability to donate electron was adopted as a model for GQD along with two carboxyl groups functionalized at its edges, referring it as “COOH-GQD”. Schematic presentation of GQD with TiO_2 is displayed in Fig. 5.1.

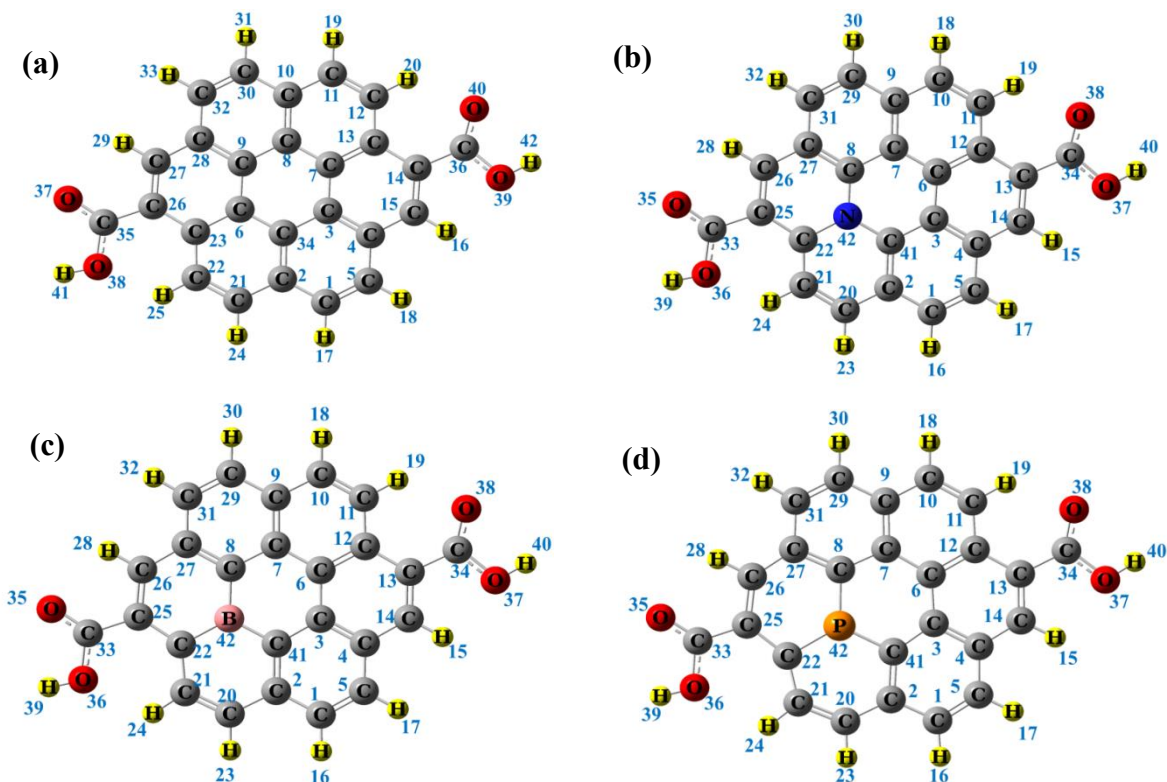


Figure 5.2: Optimized configuration of (a) carboxyl functionalized GQD (b) nitrogen doped COOH-GQD (c) boron doped COOH-GQD and (d) phosphorus doped COOH-GQD.

When photons with sufficient energy incident on GQD, it excites the electron from the HOMO level of GQD to the LUMO level which is further injected to the conduction band of electron acceptor TiO_2 either adiabatically or non-adiabatically. The carboxyl group (-COOH) functionalized at the edges of GQD is presented in Fig. 5.2 together with the substitutional doping of N, B, and P adatoms. The numbering scheme is also provided for each atom in the

optimized structures for more clarity. In the ground state structure of COOH-GQD, the bond length between carbon atoms is found to be around 1.42 Å within the GQD. The bond distance between carbon atom of –COOH– group and carbon atom is previously reported in the range of 1.48 to 1.50 Å, while oxygen atom of carboxyl group exhibits the average 1.21 Å bond length in the case of GQD [44]. In our calculation, the bond distance of 1.48 Å is found between C26 and C35, while for the case of C35 and O37 (O38) it is 1.24 Å, which in good agreement with the previous report [44].

The bond angle of 122.06° is found between carbon atoms C13, C14 and C36 for optimized GQD. Further, the repulsion between the carboxyl group and honeycomb ring reveals the rise in the angle by 2.06°. Figure 5.2 shows the outcome of doping of adatoms in carboxyl functionalized GQD. The C-C atoms bond length have been changed from 1.42 Å to 1.40 for N42-C8, 1.43 for N42-C41 and 1.45 Å for N42-C22, after substitution of carbon atom by nitrogen. However, in the case of boron substitution in COOH-GQD, the bond separation rises to 1.505 for B42-C8, 1.508 for B42-C41 and 1.54 Å for B42-C22 (Fig. 5.2(c)). Calculated C-N bond distance and C-B bond distance in doped COOH-GQD are in good agreement with previously published studies [45]. This low discrepancy in bond distances among doped adatoms is because of same atomic radii in them. However, replacement of P atom inside COOH-GQD slightly deforms the honeycomb structure of GQD by attaining the bond length of ~1.7 Å between carbon and phosphorus atoms (Fig. 5.2(d)). Substitutional doping of these three atoms has significant effect on the structure of COOH-GQD which is attributed to the variation within carbon atoms sp^2 hybridization and further may modify its electronic properties. To comprehend the interaction of COOH-GQD and adatoms with COOH-GQD, the binding energies were evaluated for all the considered geometries. The binding energy per atom has been calculated using the following equations:

For COOH-GQD

$$E_b = \frac{[nE(C)+mE(H)+ qE(O)-E(COOH-GQD)]}{42} \quad (5.8)$$

For nitrogen, boron and phosphorus adsorption over COOH-GQD

$$E_b = \frac{[nE(C)+mE(H)+ qE(O)+rE(B/N/P)-E(B/N/P-COOH-GQD)]}{42} \quad (5.9)$$

Where $E(C)$, $E(H)$ and $E(O)$ determine the total energy of carbon, hydrogen and oxygen atoms, respectively, while $E(COOH - GQD)$ and $E(B/N/P - COOH - GQD)$ are the total energies of the complex systems. The parameters n , m , and q are the number of C, H and O adatoms in all considered systems. Calculated E_b per atom for COOH-GQD and adatoms doped COOH-GQD is presented in Table 5.1. It is clear from Table 5.1 that the doping of adatoms (C/N/P) in COOH-GQD enhances E_b from 4.3 eV to 6.87 eV for COOH-GQD.

Further, B and N doped systems exhibit the almost identical binding energy per atom. The E_b is almost equivalent in case of nitrogen doped COOH-GQD and boron doped COOH-GQD attributed to the comparable ionic radii of C, N and B with minimal variation in bond-lengths among carbon-nitrogen and carbon-boron. Nonetheless, in E_b of P doping, the slightly lesser comparable value to the B and N doping can be attributed to the increase in bond length from ~ 1.42 to 1.7 \AA responsible for the distorted honeycomb structure.

Table 5.1: Computed HOMO (E_{HOMO}), LUMO (E_{LUMO}) energies, HOMO-LUMO gap (E_g), electron affinity (EA) and work function (WF) of all considered systems.

Structure	E_{HOMO} (eV)	E_{LUMO} (eV)	E_g (eV)	Binding Energy, E_b (eV)	Dipole moment (Debye)	EA	WF
COOH-GQD	-5.852	-2.375	3.47	4.3	2.40	2.375	4.11
N-COOH-GQD	-5.818	-2.429	3.38	6.87	2.43	2.429	4.12
B-COOH-GQD	-5.778	-2.368	3.41	6.84	2.65	2.368	4.07
P-COOH-GQD	-5.956	-2.610	3.34	6.72	3.16	2.610	4.28

Furthermore, it is observed that the structural changes have significant effect on the dipole moments. The calculated total dipole moment for all considered systems is presented in Table 5.1. The carboxyl group functionalized GQD comprises lowest dipole moment of 2.40 Debye among the considered systems. After doping of adatoms (nitrogen, boron and phosphorus), the dipole moment increases to 2.43, 2.65 and 3.16 Debye, respectively. For the case of P-COOH-GQD, there is an increased dipole moment due to structural distortion of honeycomb unit of

GQD at P doped site. It breaks the symmetry of π -electrons in graphene quantum dots and gives higher dipole moment compared to other doped cases. Moreover, various electronegativity values in carbon and P-COOH-GQD contribute charge redistribution and ultimately in the enhancement and generation of dipole moment [46].

5.3.2 Electronic properties

Doping effect on electronic properties are investigated by calculating HOMO and LUMO energies and E_g for all the considered systems of COOH-GQD. These are presented in Table 5.1.

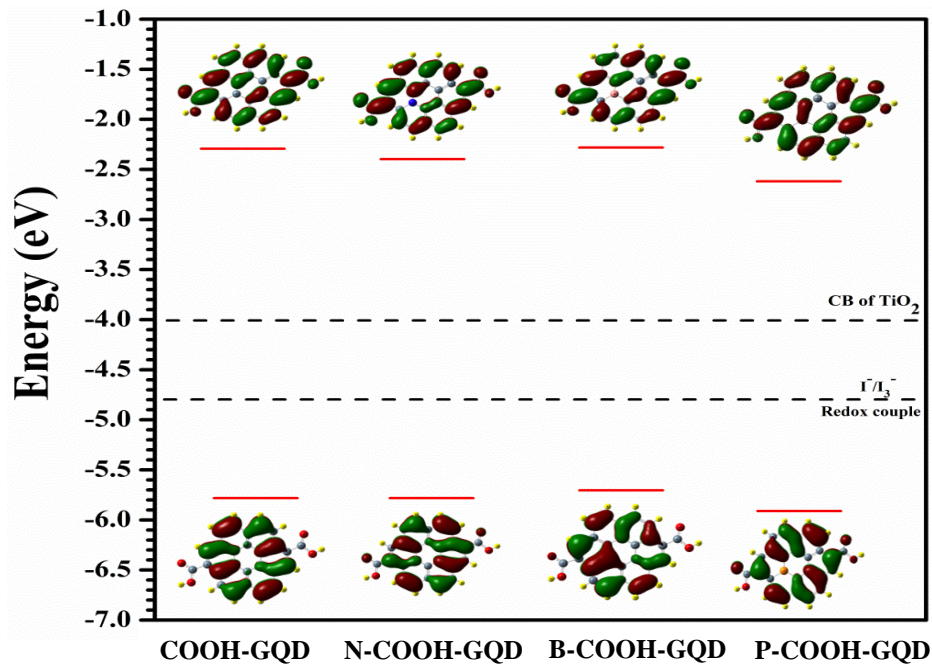


Figure 5.3: HOMO-LUMO curve for all considered systems of COOH-GQDs.

The HOMO-LUMO energy surface presented in Fig. 5.3 depicts the modification in electronic properties. A significant influence of B, N and P adatoms doping in the energy levels of HOMO and LUMO and band gap of COOH-GQD is observed. The doping reduces the band gap of COOH-GQD. The band gap follows the following order: P-COOH-GQD < N-COOH-GQD < B-COOH-GQD < COOH-GQD with magnitude 3.34 eV < 3.38 eV < 3.41 eV < 3.47 eV, respectively. It is clear from Table 5.1 that the all the considered GQD systems exhibit LUMO energies which surpasses the TiO₂ conduction band (-4.0 eV) [42]. This depicts the capability of

electron injection to CB minima of TiO₂ from the LUMO energy of pristine and doped COOH-GQD. Furthermore, the regeneration of electron-hole pair will be efficient and fast as the HOMO energies exhibit values beneath the redox couple of I⁻/I₃⁻ with magnitude of -4.8 eV [47]. Furthermore, molecular electrostatic potential (MESP) is studied to comprehend the correlation between structure and molecular activity. MESP is the potential surface which is observed by the unit positive charge in the field of molecular electron density allocation.

The chemical activity of any molecule can be identified by the MESP where, the electrophilic sites of molecules is determine by the positive potential, while the negative potential reveals the nucleophilic attack.

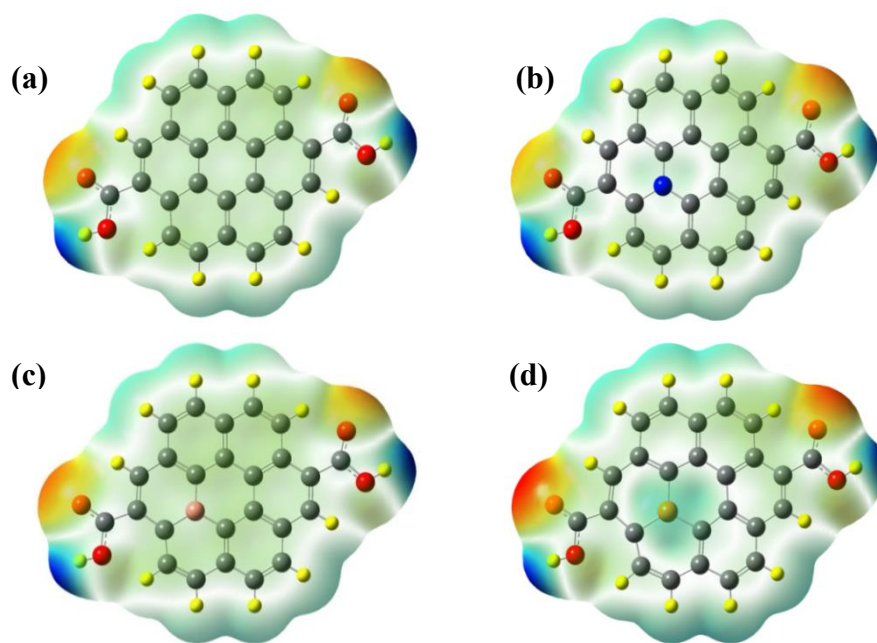


Figure 5.4: MESP surfaces for (a) carboxyl functionalized GQD (b) nitrogen doped COOH-GQD (c) boron doped COOH-GQD and (d) phosphorus doped COOH-GQD.

Mathematical representation of MESP at an instant \mathbf{r} in the molecule vicinity is determined by the following relation [48,49]:

$$\mathbf{V}(\mathbf{r}) = \sum \frac{Z_A}{|\mathbf{R}_A - \mathbf{r}|} - \int \frac{\rho(\mathbf{r}') \mathbf{d}\mathbf{r}'}{|\mathbf{r}' - \mathbf{r}|} \quad (5.10)$$

Where Z_A is the charge of nucleus having the position coordinates \mathbf{R}_A and $\rho(\mathbf{r}')$ represents electron density distribution at point \mathbf{r} . From equation (5.10), it is clear that, the net electrostatic

effect is formed at point \mathbf{r} through entire distribution of charges in the molecule. MESP for all considered COOH-GQDs systems are predicted in Fig. 5.4. Mapping of the MESP has been governed by 0.002 unit electron density for all considered systems. In Fig. 5.4 the positive electrostatic potential surfaces are determined by blue colour, while negative electrostatic potential on molecules are presented by the red colour. The order of potential in MESP is dictated as red < orange < yellow < green < blue. Zero potential region was identified by the green colour. The doping of B and P in COOH-GQD leads to the reduction in positive potential which further results in more negative electrostatic potential and shows the doped systems for superior electron injection.

The Mulliken population analysis (MPA) is also carried out to expand the understanding of charge distribution and charge transfer between adatoms and COOH-GQD (Fig. 5.5). We observed from Fig. 5.5 (a) that C and O atoms exhibit positive as well as negative charges together, while H carries positive charges solely, which is in quite good agreement with the previous reports. [50–52]. The addition of N, B and P adatoms certainly shows the transfer of charge from different H and O atoms in the dopants vicinity. The N atom exhibits the negative charge, while positive charge occurs on the B and P dopants, transfers the charge to carbon of COOH-GQD. Phosphorus exhibits positive charges among other dopants as it carries five valence electrons in its outermost shell presenting its donor nature. This leads to the considerably extended covalent atomic radius of 1.06 Å (in comparison with 0.82 Å for boron, 0.77 Å for carbon, and 0.75 Å for nitrogen) [53–55].

In addition, tuning of electronic properties by doping effect on COOH-GQD is elaborated through the calculation of work function (WF). WF is stated as the essential least energy needed to extract electron existing in the topmost occupied energy level from the solid at absolute temperature and follows the relation [56]:

$$WF = (IE + EA)/2 \quad (5.11)$$

where, IE determines the ionization potential and EA determines the electron affinity having the relation $IE = -\text{HOMO}$ and $EA = -\text{LUMO}$. Here, HOMO and LUMO energies levels were acquired from Gaussian09 distribution [29].

Table 5.1 presents the calculated work function for pristine and doped COOH-GQD. Doping of adatoms (B and P) leads to the substantial modification in work function of COOH-GQD. However, nitrogen doping in COOH-GQD reveals the identical work function to COOH-GQD. For COOH-GQD, the work function is 4.11 eV, which decreases in the case of B doping, while it shows the significant increment for phosphorus doping in COOH-GQD. The tuning of work function reveals the charge transfer between the adatoms and COOH-GQD.

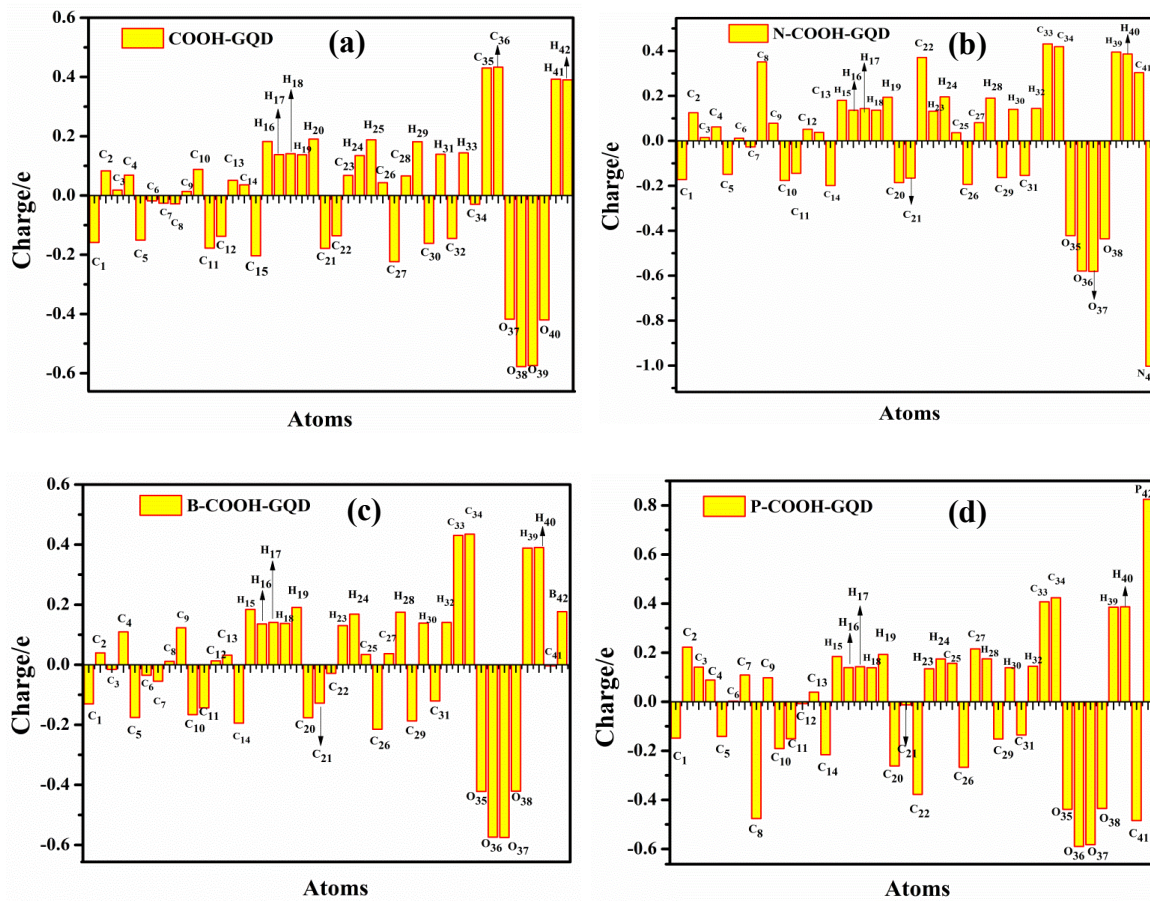


Figure 5.5: Mulliken graph for all considered systems.

5.3.3 Optical properties and solar cell parameters

Optical properties of pristine and doped COOH-GQD are investigated by calculating the UV-Vis spectra. For all considered systems UV-Vis spectra with water solvent is evaluated by utilizing the same level of theory at ten excited states. The absorption spectra of all considered systems

should fall in the region of solar spectrum, to collect more number of photon. Absorption spectra for all pristine and doped COOH-GQD systems fall into the visible range. Singlet-singlet electronic transition and its transition type are further investigated through the oscillator strength. Capabilities of absorption and emission transitions among orbital energies depict the oscillator strength presented in Table 5.2. [58].

Table 5.2: Evaluated maximum absorption wavelength, λ_{\max} (nm), electronic transition energy (eV), oscillator strength (f) and light harvesting energy (LHE) of all systems.

Structure	λ_{\max} (nm),	Energy (eV)	f	LHE
COOH-GQD	316	3.93	0.77	0.83
N-COOH-GQD	444	2.79	0.08	0.16
B-COOH-GQD	440	2.82	0.088	0.183
P-COOH-GQD	456	2.72	0.107	0.21

The electronic transition H-1→LUMO (12%) and HOMO→L+1 (78%) considerably participates in the maximum peak wavelength with highest oscillator strength, while H-2→L+2 (3%) and H-1→L+1 (2%) transitions shows low contribution to the absorption, which are in good agreement with the closed shell carboxyl functionalized GQD [13]. Above intense transition is defined as $n\rightarrow\pi^*$ transition expected from the C=O. Further, doping of adatoms in COOH-GQD modulates the optical properties as can be seen form Fig. 5.6.

The broad peak is observed in UV-Vis spectra at 316 nm along with one shoulder peak present at 400 nm for COOH-GQD, which is quite equivalent with experimental studies [59, 60]. A minor difference with the experimental wavelengths is attributed to several parameters, for instance, concentration of COOH group in GQD edges. Additionally, the properties of GQDs are very sensitive to its size and shape resulting in expected shift in the peak further modifying its electronic and optical properties [61].

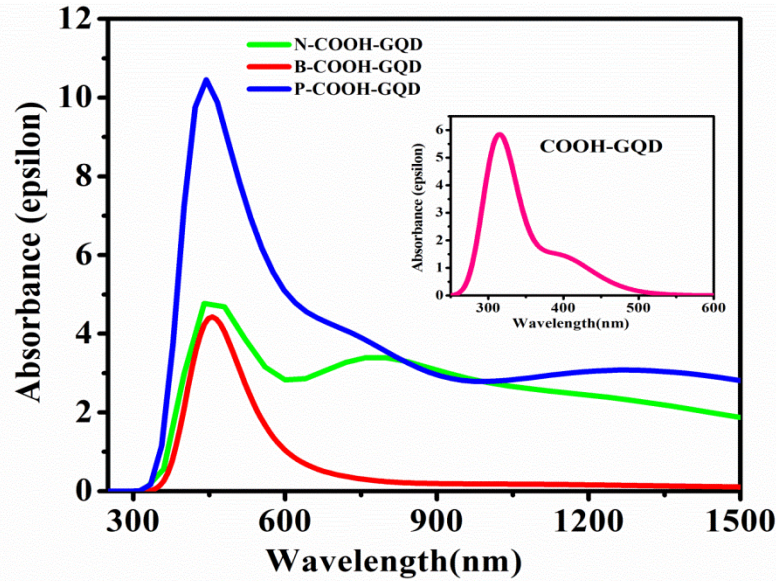


Figure 5.6: UV-Vis curve of all considered systems.

After doping of adatoms in COOH-GQD, red shift is observed in the 361 nm peak with order of magnitude: 361 nm < 440 nm < 444 nm < 456 nm in systems COOH-GQD < B-COOH-GQD < N-COOH-GQD < P-COOH-GQD, respectively and contains the identical trend with previous theoretical result [17]. The observed red shift might be occurred due to the larger atomic radius and more number of valence electrons in N and P atoms compare to carbon, further reveals the tailoring of electronic excitation properties of COOH-GQD. In case of phosphorous doping, intense absorption peak is observed at 456 nm which is higher compared to considered systems, consequently, presenting superior LHE at larger wavelengths [62]. These results in the development in the PCE of solar cells made-up of P doped COOH-GQD. With the help of Tauc relation (following equation 5.12), optical band gap is obtained for pristine and doped COOH-GQD systems and presented in Fig. 5.7:

$$\alpha h\nu \approx (h\nu - E_g)^n \quad (5.12)$$

Here, α determines the absorption coefficient, E_g defines the energy band gap, and $h\nu$ denotes the incident photon energy. Tauc plots for all considered systems where $(\alpha h\nu)^2$ is plotted with incident photon energy ($h\nu$) reveals the direct allowed transition in comprising the significant solar energy harvesting [64]. For COOH-GQD, the obtained optical band gap from Tauc plot is

3.51 eV, that further decreases after doping of nitrogen, boron and phosphorus atoms in COOH-GQD to 2.04 eV, 2.15 eV and 2.09 eV, respectively, having an excellent agreement with the previous reports [59,60]. The reduced optical bandgap after doping of adatoms extends its implementation towards the field of optoelectronics such as quantum dots solar cells (QDSCs). Thus, the performance of QDSCs has been checked by analytical calculation of power conversion efficiency (η) of QDSCs which relies on the solar cell parameters like V_{oc} , J_{sc} and FF. In this process, we have selected TiO_2 photo anode as charge collector material possessing excellent performance with photovoltaic devices, low cost power production, economically reliable and most importantly its environmental friendly nature. [65,66]. Moreover, experimental

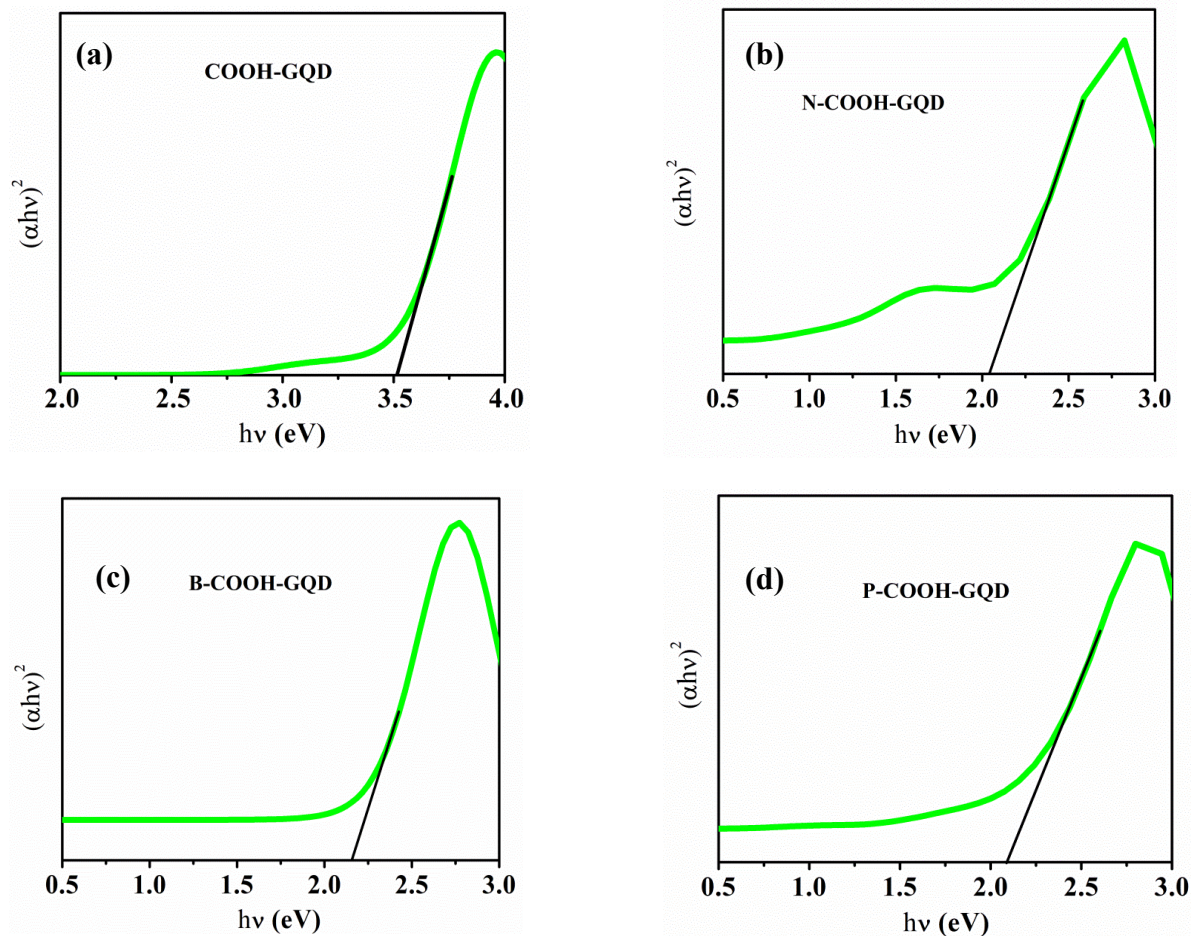


Figure 5.7: Tauc plot of all considered systems.

analysis shows that the charge injection from GQD to TiO₂ is significantly better after synthesis of GQD on TiO₂ [67]. In addition, presence of π -electron in GQD reveals the superior compatibility between GQD and TiO₂ system further accelerating the charge between the junction formed by donor and acceptor. Previous study on GQD with TiO₂ determines that the functional groups may enhance the unification of electronic properties. [67]. In the present study, the connection between COOH-GQD and TiO₂ surface will be formed by the functional group –COOH– attached with GQD at the edges for transition of electron to TiO₂ surface. Furthermore, the LUMO energy of all considered systems occupies the higher values than the CBM of TiO₂ surface, which speed ups the electronic transition from excited state of GQDs to CBM of TiO₂. On the other hand, the recombination process of electron hole pair is effectively faster as the obtained E_{HOMO} falls beneath the I⁻/I₃⁻ redox couple. Various researches have been conducted on the nano allotropes of carbon such as graphene, carbon nanotubes, GQDs etc. using TiO₂ as electron transport layer because of its wide solar light spectrum and quick charge separation capabilities [67–69]. In present investigation, the energy levels of electrons in COOH-GQD were modulated by doping of adatoms further providing rise to the splitting of charges and hot electron injection on TiO₂. Thus, we have selected TiO₂ nano-crystalline surface as charge transport material for GQDs solar cells as the LUMO energy of TiO₂ is below the LUMO energy of doped as well as undoped COOH-GQD [47]. This significantly enhances the injection of electron to TiO₂ from the doped/undoped GQD leading to the increase in efficiency of QDSCs. Before moving to the efficiency, the optical parameters such as maximum absorption wavelength (λ_{\max}), electronic transition energy, oscillator strength (f) and light harvesting energy (LHE), which plays important roles in power conversion efficiency (PCE) is presented in Table 5.2. The LHE totally depends on the oscillator strength having the following relation [70]:

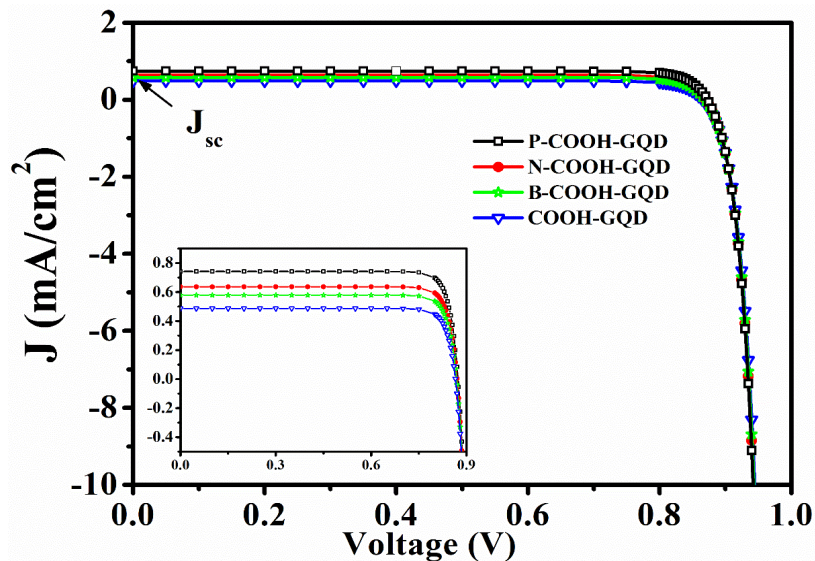
$$LHE = 1 - 10^{-f} \quad (5.13)$$

Here, TD-DFT calculations were utilized to evaluate the oscillator strength. LHE for all the system is found to be in the following order: COOH-GQD > P-COOH-GQD > B-COOH-GQD > N-COOH-GQD. A minor variation in LHE in case of doped COOH-GQD give rise to almost identical photo currents in solar cells. The calculated solar cell parameters are presented in Table 5.3.

Table 5.3: Computed solar cell parameters of systems.

Structure	V_{oc} (eV)	FF	J_{sc} (mA/cm ²)	η (%)
COOH-GQD	1.625	0.918	0.474	0.7
N-COOH-GQD	1.571	0.916	0.596	0.86
B-COOH-GQD	1.632	0.919	0.579	0.87
P-COOH-GQD	1.39	0.908	0.721	0.909

The open circuit voltage is a crucial parameter for solar cell having the direct relation with the LUMO level of donor (GQD systems) and TiO₂ conduction band and was theoretically obtained using relation (5.2) [7]. Modification in LUMO level of COOH-GQD by doping of adatoms leads in the tailoring the value of V_{oc} . Our calculated values of V_{oc} fall in the range of 1.39 to 1.63 eV. Further, the essential charge transfer will occur for both pristine and doped COOH-GQD as the obtained values of V_{oc} are positive [7]. The current-voltage analysis is determined by the J-V curve and it is presented in Fig. 5.8 of all COOH-GQD systems.

Figure 5.8: Evaluated J-V curve at temperature $T=300K$.

It is clear from the Fig. 5.8 that P doped COOH-GQD exhibits the highest value of J_{sc} among all considered systems. Here, the total current density has been calculated by the relation given [71]:

$$J = J_{sc} - J_0 \left(e^{\frac{qV}{kT}} - 1 \right) \quad (5.14)$$

Where J_0 is total of all regeneration mechanisms like the Shockley-Read-Hall (SRH), surface, contact and Auger recombination mechanisms and known as saturation current density [72].

For the pristine COOH-GQD, the obtained values of J_{sc} , FF and efficiency are 0.47 mA/cm^2 , 0.91 and 0.7%, respectively. Further, inclusion of nitrogen in COOH-GQD gives rise to the efficiency 0.86%, having an increment in efficiency of COOH-GQD by $\approx 22.8\%$, which is quite higher than earlier reported nitrogen doped carbon dots [16]. In addition, efficiency of COOH-GQD has enhanced by $\sim 30\%$ in case of phosphorus doping and achieved 0.909% PCE. This significant enrichment in efficiency was featured by efficient injection of electrons in case of phosphorus doped COOH-GQD to TiO_2 . The present work recommends that the doping of adatoms such as P and N can significantly enhance the efficiency of QDSCs based on GQDs [73].

5.4 Conclusions

In this chapter, a systematic theoretical investigation was carried out to understand the results of substitutional doping on solar energy conversion efficiency for carboxyl group functionalized GQD. The PCE of COOH-GQD has shown significant enhancement up to 30% after doping of adatoms by modulating the electronic and optical properties. Further, the energy levels HOMO and LUMO considerably changed after doping results in excellent photovoltaic behavior of COOH-GQD. The interaction of COOH-GQD and adatoms is significantly given by the binding energy calculation which will be utilized for designing the solar cells based on GQDs. The P-COOH-GQD possess added light harvesting efficiency as it exhibits intense UV-Vis absorption at 450 nm wavelength. Further, the inclusion of adatoms in COOH-GQD leads to the reduced band gap in doped COOH-GQD presenting significant application in optoelectronics. The P-COOH-GQD reveals the greater value of V_{oc} with TiO_2 surface leading the notable injection of electron from donor to TiO_2 surface. The PCE for all systems are in the order of: phosphorus doped COOH-GQD > boron doped COOH-GQD > nitrogen doped COOH-GQD > pristine COOH-GQD. Our approach of doping in COOH-GQD determines the significant importance for development of next generation quantum dot solar cells based on GQDs.

References

1. R. Singh, G. F. Alapatt, G. Bedi, *Electronics and Energetics* **27** (2014) 275-298.
2. O. E. Semonin, J. M. Luther, S. Choi, H. Y. Chen, J. Gao, A. J. Nozik and M. C. Beard, *Science* **334** (2011) 1530-1533.
3. I. J. Kramer, E. H. Sargent, *Chem. Rev.* **114** (2013) 863-882.
4. M. R. Kim, D. Ma, *J Phys Chem Lett* **6** (2014) 85-99.
5. E. M. Barea, M. Shalom, S. Giménez, I. Hod, I. Mora-Seró, A. Zaban, J. Bisquert, *J. Am. Chem. Soc.* **132** (2010) 6834-9.
6. R. S. Selinsky, Q. Ding, M. S. Faber, J. C. Wright, S. Jin, *Chem. Soc. Rev.* **42**, (2013) 2963-2985.
7. S. K. Muzakir, N. Alias, M. M. Yusoff, J. Rajan, *Phys. Chem. Chem. Phys.* **15** (2013) 16275-16285.
8. T. Sogabe, Q. Shen, K. Yamaguchi, *J. Photon. Energy* **6**, (2016) 040901-040928.
9. M. Kouhnavard, S. Ikeda, N. A. Ludin, N. B. Ahmad Khairudin, B. V. Ghaffari, M. A. Mat-Teridi, M. A. Ibrahim, S. Sepeai, K. Sopian, *Renew. Sustain. Energy Rev.* **37** (2014) 397-407.
10. M. R. Kim, D. Ma, *J. Phys. Chem. Lett.* **6** (2015) 85-99.
11. S. Bak, D. Kim, H. Lee, *Curr. Appl. Phys.* **16** (2016) 1192-1201.
12. Z. Pan, H. Rao, I. Mora-Seró, J. Bisquert, X. Zhong, *Chem. Soc. Rev.* **47** (2018) 7659-7702.
13. D. Sharma, R. Jha, S. Kumar, *Sol. Energy Mater. Sol. Cells* **155** (2016) 294-322.
14. M. Bacon, S. J. Bradley, T. Nann, *Part. Part. Syst. Charact.* **31** (2014) 415-428.
15. Y. Q. Zhang, D. K. Ma, Y. G. Zhang, W. Chen, S. M. Huang, *Nano Energy* **2**, 545-552 (2013).
16. H. Wang, P. Sun, S. Cong, J. Wu, L. Gao, Y. Wang, X. Dai, Q. Yi, G. Zou, *Nanoscale Research Letters* **11**, 27 (2016).
17. J. Feng, H. Dong, B. Pang, F. Shao, C. Zhang, L. Yu, L. Dong, *Phys. Chem. Chem. Phys.* **20**, (2018) 15244-15252.

18. G. Konstantatos, M. Badioli, L. Gaudreau, J. Osmond, M. Bernechea, F. P. G. Arquer, F. Gatti, F. H. Koppens, *Nat. Nanotechnol.* **7**, (2012) 363-368.
19. D. Chao, C. Zhu, X. Xia, J. Liu, X. Zhang, J. Wang, P. Liang, J. Lin, H. Zhang, Z. X. Shen, H. J. Fan, *Nano Lett.* **15**, (2015) 565- 573.
20. M. F. Budyka, *Spectrochim Acta A Mol Biomol Spectrosc* **207** (2019) 1-5.
21. V. Sharma, N. Som, S. D. Dabhi, P. K. Jha, *ChemistrySelect* **3** (2018) 2390-2397
22. A. C. Grimsdale, K. Müllen, *Angew. Chem. Int. Ed.* **44** (2005) 5592-5629.
23. K. Müllen, J.P. Rabe, *Acc. Chem. Res.* **41** (2008) 511-520.
24. A. Narita, X. Y. Wang, X. Feng, K. Müllen, *Chem. Soc Rev.* **44** (2015) 6616-6643.
25. B. Yuan, X. Sun, J. Yan, Z. Xie, P. Chen, S. Zhou, *Phys. Chem. Chem. Phys.* **18** (2016) 25002-25009.
26. J. P. A. de Mendonca, A. H. de Lima, G. M. A. Junqueira, W. G. Quirino, C. Legnani, I. O. Maciel, F. Sato, *Mater. Res. Express* **3** (2016) 055020.
27. A. D. Becke, *Phys. Rev A* **38** (1988) 3098-3100.
28. C. Lee, W. Yang, R.G. Parr, *Phys. Rev. B* **37** (1988) 785-789.
29. M. J. Frisch et al. GAUSSIAN 09 (Revision C.01), Gaussian, Inc., Wallingford, CT, 2010.
30. G. Scalmani, M. J. Frisch, *J. Chem. Phys.* **132** (2010) 114110.
31. E. Cances, B. Mennucci, J. Tomasi, *J. Chem Phys.* **107** (1997) 3032-3041.
32. J. Tomasi, M. Persico, *Chem. Rev.* **94** (1994) 2027-2094.
33. J. Tomasi, B. Mennucci, R. Camm, *Chem. Rev.* **105** (2005) 2999-3093.
34. L. Yu, A. Zunger, *Phys. Rev. Lett.* **108** (2012) 068701-5.
35. E. Alamy, A. Bourass, M. Amine, A. Hamidi, M. Bouachrine, *Karbala Int. J. of Mod. Sci.* **3** (2017) 75-82.
36. M. A Green, A. Ho-Baillie, H. J Snaith, *Nat. Photon.* **8** (2014) 506-514.
37. W-J Yin, T. Shi, Y. Yan, *Adv. Matter.* **26** (2014) 4653-8.
38. M. A. Green, *Solid-State Electronics* **24** (1981) 788-789.
39. A. Mihi, F. J. López-Alcaraz, H. Míguez, *Appl. Phys. Lett.* **88** (2006) 193110-3.
40. C.-A. Tao, W. Zhu, Q. An, G. Li, *J. Phys. Chem. C* **114** (2010) 10641-10647.

-
41. M. Guo, K. Xie, J. Lin, Z. Yong, C. T. Yip, L. Zhou, Y. Wang, H. Huang, *Energy Environ Sci.* **5** (2012) 9881-9888.
 42. D. Cahen, G. Hodes, M. Grätzel, J.F. Guillemoles, I. Riess, *J. Phys Chem B* **104**, (2000) 2053-2059.
 43. N. N. Som, P. M. W. P. Sampath, S. D. Dabhi, V. Mankad, S. Shinde, M. L. C. Attygalle, P. K. Jha, *Solar Energy* **173** (2018) 1315-1322.
 44. M. Baranska, K. Chruszcz, A.B. Boduszek, L.M. Proniewicz, *Vib. Spectrosc.* **31** (2003) 295–311.
 45. F. Montejo-Alvaro, J. Oliva, M. Herrera-Trejo, H. M. Hdz-García, A. I. Mtz-Enriquez, *Theoretical Chemistry Accounts* **138** (2019) 1-15.
 46. J. Beheshtian, A. Sadeghi, M. Neek-Amal, K. H. Michel, F. M. Peeters, *Phy. Rev. B* **86** (2012) 195433-8.
 47. A.G. Al-Sehemi, A. Irfan, A.M. Asiri, Y. A. Ammar, *Spectrochim. Acta A* **91** (2012) 239-242.
 48. B. Galabov, P. Bobadova-Parvanova, *J. Phys. Chem. A* **103** (1999) 6793-6799.
 49. J. Goldwasser, J. S. Murray, P. Politzer, In *The Molecular Electrostatic Potential: A Tool for Understanding and Predicting Molecular Interaction* (Fort Belvoir: DTIC-Defense Technical Information Center) 1998.
 50. M. Drissi, N. Benhalima, Y. Megrouss, R. Rachida, A. Chouaih, F. Hamzaoui, *Molecules* **20** (2015) 4042-4054.
 51. D. Sharma, S. N. Tiwari, *Int. J. Electroactive Mater.* **5** (2017) 19-30.
 52. P. Govindasamy, S. Gunasekaran, S. Srinivasan, *Spectrochim Acta A Mol Biomol Spectrosc* **130** (2014) 329-336.
 53. V. Strelko, V. Kuts, P. Thrower, *Carbon* **38** (2000) 1499-1503.
 54. S. Some, J. Kim, K. Lee, A. Kulkarni, Y. Yoon, S. Lee, T. Kim, H. Lee, *Adv. Mater.* **24** (2012) 5481-6.
 55. M. P. Mitoraj, A. Michalak, *Inorg. Chem.* **49** (2010) 578-582.
 56. V. Sharma, S. D Dabhi, S. Shinde, P. K Jha, *AIP Conference Proceedings* **1961**, (2018) 030031-6.

-
57. A. Hlel, A. Mabrouk, M. Chemek, I. B. Khalifa, K. Alimi, *Computational Condensed Matter* **3** (2015) 30-40.
58. W. Demtröder, *Laser Spectroscopy: Basic Concepts and Instrumentation*. Springer. p. 31. (2003).
59. J. Ali, G. Siddiqui, Y. J. Yang, K. T. Lee, K. Um, K. H. Choi, *RSC Advances* **6** (2016) 5068-5078.
60. D. Bhatnagar, S. Singh, S. Yadav, A. Kumar, I. Kaur, *Mater. Res. Express* **4** (2017) 015101.
61. P. Tian, L. Tang, K. S. Teng, S. P. Lau, *Mater Today Chem* **10** (2018) 221-258.
62. N. Santhanamoorthi, C-M. Lo, J-C. Jiang, *J. Phys. Chem. Lett.* **4** (2013) 524-530.
63. J. Tauc, R. Grigorovici, A. Vancu, *Phys. Stat. Sol.* **15** (1966) 627-636.
64. V. H. Nguyen, H. Y. Chan, J. C. S. Wu, *J. Chem. Sci.* **125** (2013) 859-867.
65. Y. Bai, I. Mora-Seró, F. De Angelis, J. Bisquert, P. Wang, *Chem. Rev.* **114** (2014) 10095-10130.
66. M. Kutraleeswaran, M. Venkatachalam, M. Saroja, P. Gowthaman, S. Shankar G. Parthasarathy, J. Sounder, *Journal for Advance Research in Applied Sciences* **5**, 453-474 (2018).
67. R. Long, D. Casanova, W-H Fang, O. V. Prezhdo, *J. Am. Chem. Soc.* **139** (2017) 2619-2629.
68. K. J. Williams, C. A. Nelson, X. Yan, L.-S. Li, X. Zhu, *ACS Nano* **7** (2013) 1388-1394.
69. Z. Salam, E. Vijayakumar, A. Subramania, N. Sivasankar, S. Mallick, *Sol. Energy Mater. Sol. Cells* **143** (2015) 250-259.
70. M. Xie, J. Wang, H-Q. Xia, F-Q. Bai, R. Jia, J-G. Rim, H-X. Zhang, *RSC Advances* **5** (2015) 33653-33665.
71. M. Bercx, N. Sarmadian, R. Saniza, B. Partoens, D. Lamoen, *Phys. Chem. Chem. Phys.* **18** (2016) 20542-20549.
72. X. Huang, H. Fu, H. Chen, Z. Lu, D. Ding, Y. Zhao, *J. Appl. Phys.* **119** (2016) 213101-7.
73. V. Sharma, P. K. Jha, *Sol. Energy Mater. Sol. Cells* **200** (2019) 109908.